Petroleum Science 23 (2026) 332–349

Contents lists available at ScienceDirect

Petroleum Science

journal homepage: www.keaipublishing.com/en/journals/petroleum-science

Original Paper

A novel semi-analytical model for pressure transient analysis of fault-controlled fractured-caved gas reservoirs and field applications

Pin Jia *, Quan-Yu Pan, Jia Li, Jiang-Peng Hu, Yu-Cheng Wu, Lin-Song Cheng

College of Petroleum Engineering, China University of Petroleum (Beijing), Beijing, 102249, China

ARTICLE INFO

Article history:
Received 15 February 2025
Received in revised form
28 October 2025
Accepted 2 November 2025
Available online 7 November 2025

Edited by Yan-Hua Sun

Keywords:
Semi-analytical model
Fault-controlled fractured-caved gas reservoirs
Pressure transient analysis
Large-scale caves
Point source solution

ABSTRACT

Fractured-caved gas reservoirs are widely distributed and hold substantial reserves in northwestern China, showing considerable development potential. However, their strong heterogeneity and significant variations present challenges. Conventional multi-media well test interpretation models are not well-suited to fractured-caved gas reservoirs, while more suitable numerical models often require lengthy modeling times and extensive computations. To address these limitations, this paper introduces an efficient semi-analytical well test interpretation model adaptable to various fracture–cave combinations. This model integrates methods such as fluid flow and storage flow theory, the point source solution method, and multi-parameter optimization. Results demonstrate that for different wellbore–fracture–cave configurations, the point source solution method requires only the construction of a coupled solution matrix for each unit to obtain the pressure and flow rate distributions, significantly reducing the workload associated with model setup and solution. Additionally, applying the semi-analytical models to typical wells in the Shunbei field yielded strong fitting accuracy and effectively inverted key parameters related to the wellbore, fracture regions, and caves. The models developed in this paper provide valuable guidance for the efficient development of fractured-caved reservoirs.

© 2026 Publishing services by Elsevier B.V. on behalf of KeAi Communications Co. Ltd. This is an open access article under the CC BY-NC-ND license (http://creativecommons.org/licenses/by-nc-nd/4.0/).

1. Introduction

In fractured-caved carbonate reservoirs, caves, fracture regions, and matrix serve as the three primary storage spaces (Ahmadi et al., 2014; Mohammed et al., 2021; Tang et al., 2023). Notable examples of these reservoirs include the Tahe oilfield, Tarim Ordovician reservoirs, and the Liuhua oilfield, South China Sea. These reservoirs predominantly feature large caves and fractures as the main storage and flow spaces, with pore sizes that can reach meters in scale (Gao et al., 2016; Wu et al., 2022; Zhao et al., 2014). Their storage and flow characteristics exhibit significantly more complex flow mechanisms compared to sandstone and fractured carbonate reservoirs. Fractured-caved reservoirs exhibit considerable spatial scale variability, with discrete cave distributions and intricate combinations of fracture regions and caves. This multi-scale nature results in complex flow dynamics, with diverse flow patterns within fractured-caved units and ambiguous mechanisms governing fluid exchange between the media. For example, based on fluid dynamics principles, fluid flow within large pores is classified as free flow (Golfier et al., 2015; Loucks, 1999; Yang et al., 2024). As a result, conventional dual-, triple-, or multi-porosity well test interpretation models are often unsuitable for fractured-caved reservoirs, as they struggle to accurately represent and interpret parameters related to fracture regions and caves.

The challenge of modeling such reservoirs builds upon many studies of fractured systems. Foundational work, such as the dual-porosity model by Warren and Root (1963), provided the first conceptual framework for reservoirs with two distinct media. Modern well test interpretation has been profoundly shaped by the use of the pressure derivative, a technique pioneered by Bourdet et al. (1989) that greatly enhances the ability to diagnose flow regimes. As comprehensively reviewed by Gringarten (2008), the field has continuously evolved towards models that can more accurately capture reservoir complexity. For the fractured-caved reservoirs central to this study, extensive research has been conducted on well test interpretation models for these complex fracture–cave combinations. Current models for fracture flow can be divided into two main categories: analytical models and numerical models. Analytical models seek to establish simple

* Corresponding author.
E-mail address: jiapin1990@163.com (P. Jia).
Peer review under the responsibility of China University of Petroleum (Beijing).

https://doi.org/10.1016/j.petsci.2025.11.002
1995-8226/© 2026 Publishing services by Elsevier B.V. on behalf of KeAi Communications Co. Ltd. This is an open access article under the CC BY-NC-ND license (http://creativecommons.org/licenses/by-nc-nd/4.0/).

analytical expressions. Consequently, caves are generally treated as either high-permeability bodies or equipotential bodies. In high-permeability body models, caves are represented as highly permeable porous media, facilitating the development of mathematical flow models for well test interpretation. However, since most large caves are unfilled, the flow within them does not adhere to Darcy's law and instead follows free-flow behavior characteristic of such caves. Consequently, representing caves as high-permeability bodies can overlook the unique properties of unfilled caves, resulting in inaccuracies in well test pressure response curves (Liu, 2020).

The equipotential body model assumes that pressure within a cave propagates rapidly to its boundaries, reaching pseudo-steady state, making the model suitable for caves with extremely high permeability. In this approach, caves are treated as zero-dimensional units with uniform internal pressure during flow. Liu (2020) applied an equipotential body model to represent caves and modeled flow in the fracture region as one-dimensional unsteady flow, resulting in a well test model designed for one-dimensional fractured-caved reservoirs. Wei et al. (2022) developed a multi-cave, multi-fracture zone model for vertical bead-string wells, incorporating four media types: large caves, small caves, high-angle structural fractures, and matrix. Flow within fracture zones follows Darcy's law, while flow within large caves follows free flow. Ai et al. (2023) proposed two mathematical models for acid fracturing well testing in carbonate reservoirs, treating caves as equipotential media and coupling acid-fracture flow, fracture flow, and cave flow.

Numerical models provide a more precise and visually illustrative representation of the position and shape of fractured-caved reservoirs, enabling more accurate simulation of fluid flow in porous media. To achieve this, sophisticated numerical approaches are used, such as discrete fracture network (DFN) models that explicitly map fracture connectivity (Karimi-Fard, 2004) or coupled-physics models that solve for both Darcy flow in the matrix and Stokes/Brinkman flow in open conduits. However, the flexibility and computational accuracy of numerical simulation models come at the cost of significant computational resources. Flow coupling is achieved through boundary continuity conditions, yielding a comprehensive flow model (Arbogast and Gomez, 2009; Huang et al., 2020). Lin et al. (2007) introduced a coupled model of pipe flow and Darcy flow, conceptualizing fractured-caved reservoirs as alternating cave and fracture units. They described cave flow using pipe flow and fracture flow using Darcy's law, and constructed a linear flow physical model solved through numerical methods. Xu et al. (2023) embedded randomly generated natural fractures into reservoirs, developing a 3D numerical model for oil–water two-phase flow in fractured-caved reservoirs. They employed the Hagen–Poiseuille law to describe cave fluid flow, effectively coupling interactions between fractures, caves, and matrix. Li et al. (2023) developed a numerical model integrating a continuous medium with vugs to examine vug impacts on transient pressure response. Although numerical models depict fluid flow with high accuracy in complex media, their extensive computational requirements limit their practicality for engineering applications. Current fractured-caved well test models are relatively limited in their applicability and lack suitability for a broader range of fractured-caved reservoir types.

To clearly position the contribution of this work, we provide a focused comparison with existing approaches in Table 1. While numerical models (e.g., Xu et al., 2023) offer high precision, they suffer from significant computational inefficiency and complex grid generation, limiting their use in routine well test interpretation. Conversely, traditional analytical models (e.g., Liu, 2020) are computationally fast but lack the flexibility to represent the diverse fracture–cave combinations found in fields like Shunbei. Recent semi-analytical models have improved this, but often require case-by-case model derivation (Pan et al., 2024). The primary contribution of this paper is the development of a semi-analytical framework that provides a unified treatment of wellbore, fracture, and cave elements. By using a modular, point-source-based matrix solution, our method allows for the flexible assembly of arbitrary configurations (as demonstrated for all six scenarios in Fig. 8) without re-deriving governing equations. This unique combination of flexibility and computational efficiency significantly reduces the modeling workload and provides a practical tool for the rapid interpretation of pressure transient data in complex fault-controlled reservoirs.

2. Physical model

The reservoirs in the Shunbei field are representative of fault-controlled, fractured-caved gas systems characterized by a distinct storage-conduit duality. Large-scale karst caves, often appearing as beaded reflections on seismic profiles, serve as the dominant storage medium. In contrast, fractures primarily function as high-permeability conduits that connect these caves and facilitate fluid flow, while contributing slightly to the overall storage capacity. This complex geological structure, confirmed by

Table 1
Comparative analysis of the proposed model and representative existing models.

Model	Model flexibility	Unified treatment	Computational efficiency	Modeling workload	Applicability example
Representative numerical model (e.g., Xu et al., 2023)	High (handles complex geometries)	No (different grids for free and Darcy flow)	Low (requires extensive meshing and long computation time)	High (complex grid generation)	Simulates detailed physics in a single complex scenario
Representative analytical model (e.g., Liu, 2020)	Low (limited to simple, idealized geometries)	No (separate derivations for different configurations)	High (fast analytical solution)	Low (simple setup)	Models a single W–F or W–C system
Representative semi-analytical model (e.g., Pan et al., 2024)	Medium (often targets specific configurations)	Partial (may require new derivations for novel configurations)	Medium (faster than numerical model, slower than purely analytical model)	Medium (derivation can be complex)	Analyzes W–F, W–F–C, W–C–F, and W–C–F–C system
Proposed model in this work	Medium (handles arbitrary wellbore–fracture–cave combinations via matrix assembly)	Yes (well, fracture, and cave treated as consistent, modular units)	Medium (matrix solution is non-iterative and extremely fast)	Low (requires only matrix definition, avoids re-derivation)	Can model all scenarios in Fig. 8 within a single unified framework

extensive core and well-logging data, results in highly heterogeneous reservoirs with complex flow dynamics.

The spatial distribution and connectivity of these fractured-caved systems are structurally controlled by large-scale strike-slip faults. These faults serve a dual role, acting as both high-permeability flow pathways and as boundaries that define lengthened fracture corridors. Fracture regions typically develop parallel to the fault planes, and extensive dissolution often forms large caves along these corridors. A conceptual schematic of this fault-controlled geological setting is illustrated in Fig. 1.

Based on the geological characteristics of the Shunbei field, four typical combination patterns of wellbore, caves, and fracture regions are summarized in Table 2.

(1) Wellbore–fracture model: This represents a scenario where the wellbore is directly connected to a fracture region, and no large-scale caves are encountered nearby.
(2) Wellbore–fracture–cave model: This pattern describes a wellbore connected to a fracture, which in turn communicates with a single, far-end cave.
(3) Wellbore–cave–fracture model: This describes a case where the wellbore directly penetrates a large-scale cave, which is then connected to an adjacent fracture region.
(4) Wellbore–cave–fracture–cave–fracture model: This represents a complex series or 'bead-on-a-string' configuration, where the well penetrates a near-well cave that is connected via a fracture to a second, more distant cave system.

3. Mathematical models of fluid flow

In this section, a semi-analytical model is developed for the complex wellbore–fracture–cave configurations identified previously. The model solution is derived in the Laplace domain and inverted numerically to generate type curves. These curves are then used to identify characteristic flow regimes and analyze the underlying flow mechanisms. The wellbore–cave–fracture–cave–fracture configuration, shown schematically in Fig. 2, is used as the primary example to illustrate the model's formulation.

The model is based on the following key assumptions: (1) The reservoir contains a single-phase gas. (2) A single vertical well produces at a constant rate. (3) Wellbore storage and skin effects are considered. (4) Flow within the fracture regions is characterized as one-dimensional (1D) linear flow. (5) The large-scale caves have high conductivity, allowing them to be treated as uniform-pressure equipotential bodies (Gao et al., 2016; Wei et al., 2022). (6) The transient deliverability from each cave is modeled as a storage-dominated flow (pseudo-steady state) governed by a material balance equation.

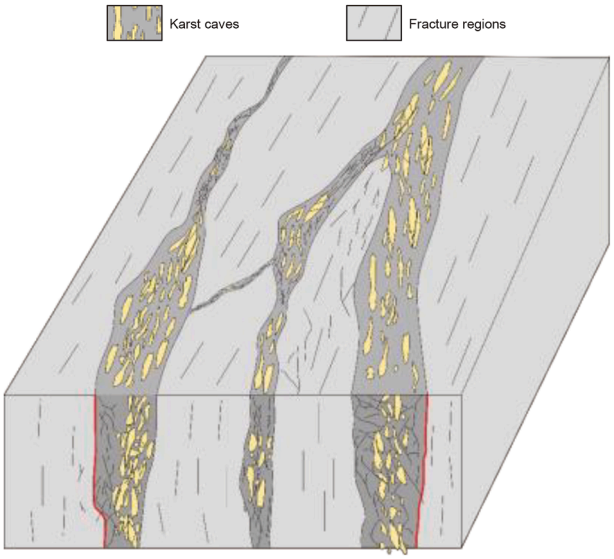

Fig. 1. Conceptual model of fault-controlled fractured-caved reservoir.

Based on the physical model and the assumptions outlined previously, the governing equations for fluid flow in the different domains can be formulated as follows.

3.1. Fluid flow in the wellbore

The equation considering the wellbore storage effect is as follows:

$$q_{sfg}B_g - q_{scg}B_g = 24V_b c_g \frac{dp_w}{dt} \tag{1}$$

where q_{sfg} is the gas reservoir sandface flow rate; q_{scg} is the ground flow rate of the gas reservoir; B_g is the gas volume coefficient; V_b is the wellbore volume; c_g is the gas compression coefficient; and p_w is the bottomhole flow pressure.

3.2. Fluid flow in cave 1

Because the cave is usually unfilled or partially filled, it has great conductivity, and the pressure in the cave propagates very rapidly. It can be considered that the pressure inside the cave is equal everywhere, and the gas is supplied outward in a pseudo-steady-state flow mode. Therefore, the flow equation of cave 1 adjacent to the wellbore is

$$q_{sfg}B_g = -24V_{c1}\phi_{c1}c_g\frac{dp_{c1}}{dt} - \frac{86.4k_{f1}w_{f1}h}{\mu_g}\frac{\partial p_{f1}}{\partial x}\bigg|_{x=x_1} \tag{2}$$

where V_{c1} is the volume of cave 1; ϕ_{c1} is the porosity of cave 1, which is usually assumed to be 1; p_{c1} is the pressure of cave 1; p_{f1} is the pressure of fracture region 1; k_{f1} is the permeability of fracture region 1; w_{f1} is the width of fracture region 1; h is the reservoir thickness; μ_g is the viscosity of gas. The left side of Eq. (2) is the supply term from the cave to the wellbore. The first term on the right side is the pseudo-steady-state flow of the cave, and the second term is the supply term from the fracture region on the right side of the cave.

3.3. Fluid flow in fracture region 1

Flow within the high-conductivity fracture region is one-dimensional. According to the assumptions, the flow can be described by Darcy's law, the governing equation for linear flow is expressed as follows:

$$\frac{1}{\partial x}\left(\frac{p_{f1}}{Z\mu_g}\frac{\partial p_{f1}}{\partial x}\right) = \frac{\phi_{f1}c_g\mu_g}{k_{f1}}\left(\frac{p_{f1}}{Z\mu_g}\frac{\partial p_{f1}}{\partial t}\right) \tag{3}$$

where Z is the gas compressibility factor; ϕ_{f1} is the porosity of fracture region 1.

The coupling between caves and fracture regions is established via pressure continuity and pseudo-steady state flow equations, where caves serve as dynamic storage units and fractures act as transmissive channels. Therefore, the pressure at the adjacent position between fracture region 1 and cave 1 is continuous:

Table 2
Physical models and seismic detection maps for typical fractured-caved reservoirs.

Reference	Region	Seismic or monitoring map	Physical model
Liao et al. (2015)	Halahatang field		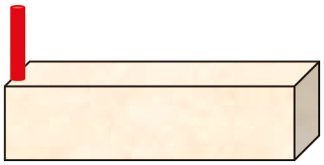
Du et al. (2022)	Shunbei field	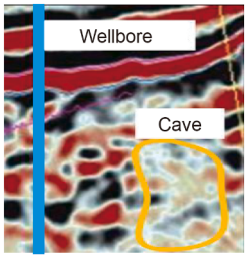	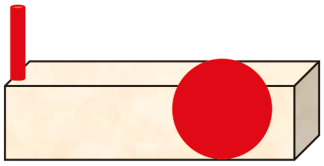
Du et al. (2019)	Shunbei field	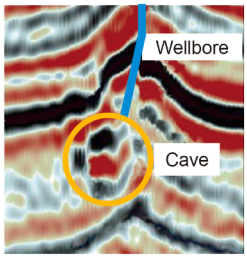	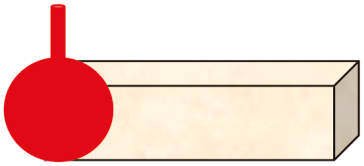
Li et al. (2021)	Shunbei field	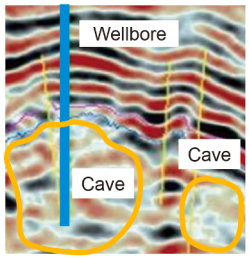	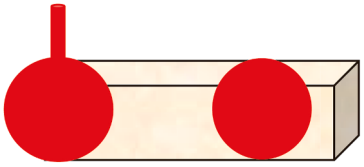

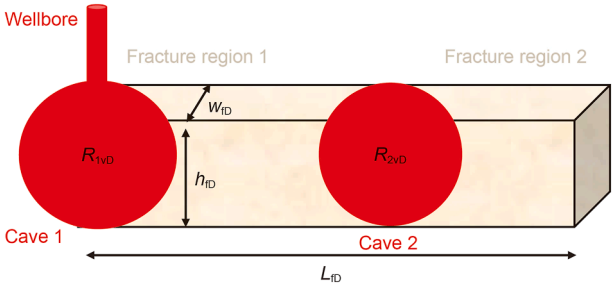

Fig. 2. Wellbore–cave–fracture–cave–fracture model.

$$p_{f1}\big|_{x=x_1} = p_{c1} \tag{4}$$

The pressure at the adjacent position between fracture region 1 and cave 2 is continuous:

$$p_{f1}\big|_{x=x_2} = p_{c2} \tag{5}$$

where p_{c2} is the pressure of cave 2.

3.4. Fluid flow in cave 2

Similar to cave 1, the gas is supplied outward in a pseudo-steady-state flow mode, so the flow equation of cave 2 is as follows:

$$\frac{86.4k_{f1}w_{f1}h}{\mu_g}\frac{\partial p_{f1}}{\partial x}\bigg|_{x=x_2} = -24V_{c2}\phi_{c2}c_g\frac{dp_{c2}}{dt} - \frac{86.4k_{f2}w_{f2}h}{\mu_g}\frac{\partial p_{f2}}{\partial x}\bigg|_{x=x_3} \tag{6}$$

where V_{c2} is the volume of cave 2; ϕ_{c2} is the porosity of cave 2, usually assumed to be 1; k_{f2} is the permeability of fracture region 2; w_{f2} is the width of fracture region 2; p_{f2} is the pressure of fracture region 2. In Eq. (6), the left side is the supply term from the cave to fracture region 1, the first term on the right side is the pseudo-steady-state flow term of the cave, and the second term is the supply term from the fracture region on the right side of the cave.

3.5. Fluid flow in fracture region 2

Similarly, the flow within fracture region 2 can be described by Darcy's law, the governing equation for linear flow is expressed as follows:

$$\frac{1}{\partial x}\left(\frac{p_{f2}}{Z\mu_g}\frac{\partial p_{f2}}{\partial x}\right) = \frac{\phi_{f2}c_g\mu_g}{k_{f2}}\left(\frac{p_{f2}}{Z\mu_g}\frac{\partial p_{f2}}{\partial t}\right) \tag{7}$$

The pressure at the adjacent part between fracture region 2 and cave 2 is continuous:

$$p_{f2}\big|_{x=x_3} = p_{c2} \tag{8}$$

The infinite boundary condition, closed boundary condition, and constant pressure boundary condition are as follows:

$$\begin{cases} p_{f2}\big|_{x\to\infty} = p_i \\ p_{f2}\big|_{x=x_4} = p_i \\ \dfrac{\partial p_{f2}}{\partial x}\bigg|_{x=x_4} = 0 \end{cases} \tag{9}$$

where ϕ_{f2} is the porosity of fracture region 2; p_i is the initial pressure or boundary pressure of the gas reservoir.

Due to the compressibility of the gas, the flow equations (Eqs. (1)–(3), (6), and (7)) are all nonlinear flow equations. The pseudo-pressure is defined as follows, and is introduced into Eqs. (1)–(9), and the equations are linearized.

$$m(p) = 2\int_{p_0}^{p}\frac{p}{Z\mu}dp \tag{10}$$

The dimensionless variables of pseudo-pressure and dimensionless time are defined to linearize and nondimensionalize Eqs. (1)–(9), and the Laplace transform is further performed to obtain the dimensionless Laplace space form of Eqs. (1)–(9), that is, the flow mathematical model of the wellbore–cave–fracture –cave–fracture model (see detailed derivations at Appendix A) is described as follows:

$$\begin{cases} 2\pi\bar{q}_{sfgD} = 2\pi sC_{c1D}\overline{m}_{c1D} + F_{c1D}\left(\dfrac{\partial\overline{m}_{f1D}}{\partial x_D}\right)_{x_D=x_{1D}} \\ \dfrac{\partial^2 m_{f1D}}{\partial x^2} = \dfrac{s}{\eta_{f1D}}\overline{m}_{f1D} \\ F_{c1D}\left(\dfrac{\partial\overline{m}_{f1D}}{\partial x_D}\right)_{x_D=x_{2D}} = -2\pi sC_{c2D}\overline{m}_{c2D} - F_{c2D}\left(\dfrac{\partial\overline{m}_{f2D}}{\partial x_D}\right)_{x_D=x_{3D}} \\ \dfrac{\partial^2\overline{m}_{f2D}}{\partial x^2} = \dfrac{s}{\eta_{f2D}}\overline{m}_{f2D} \\ \dfrac{1}{s} - \bar{q}_{sfgD} = 2\pi sC_{wD}\overline{m}_{wD} \\ \overline{m}_{f1D}\big|_{x_D=x_{1D}} = \overline{m}_{c1D} \\ \overline{m}_{f1D}\big|_{x_D=x_{2D}} = \overline{m}_{c2D} \\ \overline{m}_{f2D}\big|_{x_D=x_{3D}} = \overline{m}_{c2D} \\ \overline{m}_{f2D}\big|_{x_D\to\infty} = 0 \\ \overline{m}_{f2D}\big|_{x_D=x_{4D}} = 0 \\ \dfrac{\partial\overline{m}_{f2D}}{\partial x_D}\bigg|_{x_D=x_{4D}} = 0 \end{cases} \tag{11}$$

where s is Laplace operator; m_D is the dimensionless pseudo-pressure; t_D is the dimensionless time; η_{fD} is the dimensionless fracture hydraulic diffusivity; F_{cD} is the dimensionless fracture conductivity; C_{cD} is the dimensionless cave storage coefficient; the overbar on a variable denotes that the variable is in the Laplace domain; subscripts i, r, f, c, and g refer to initial, reference, fracture, cave, and gas, respectively.

When an early concave response appears on the derivative curve, this indicates strong cave storage behavior and supports the validity of this assumption; nevertheless, in cases of significant filling or high-velocity flow, deviations may occur and further refinement would be needed. Therefore, a potential extension of the model could incorporate non-Darcy flow mechanisms, such as Forchheimer-type corrections, to account for inertial effects if needed.

4. Model solution and verification

The mathematical model presented in Eq. (11) poses significant challenges for analytical solutions, particularly due to the complex interactions among karst caves and fracture regions. The fundamental flow mechanism of the fracture–cave combination model lies in the various configurations of three key units: the wellbore, cave, and fracture. The karst cave is treated as an equipotential body, while fracture flow is modeled as porous media flow, allowing the karst cave to be represented as a source or sink term within the fracture region. Therefore, the crux of the semi-analytical solution involves deriving the point source solution for the fracture region under different boundary conditions. By combining this with the well and cave storage solutions, a general solution can be obtained for any configuration.

In this paper, the semi-analytical approach discretizes the wellbore, fracture region, and karst cave into linear units,

employing the point source solution to establish a coupling matrix and form an efficient, semi-analytical solution. This method offers the advantage of a universal well test interpretation model that is adaptable to any wellbore–fracture–cave combination. It eliminates the need to construct unique models for each physical scenario, significantly reducing modeling effort and enhancing flexibility.

4.1. Basic solution of fracture region flow

As shown in Fig. 3, the fracture region is represented as a linear element. An analytical approach is used to derive the basic pressure solution of this linear element, assuming a source or sink of fixed strength under various boundary conditions. This allows for the construction of the source function governing flow within the fracture region.

The flow mathematical model of the fracture region under the above three different boundary conditions is as follows:

$$\begin{cases} \dfrac{\partial^2 \overline{m}_{\mathrm{fD}}}{\partial x_{\mathrm{D}}^2} = \dfrac{s}{\eta_{\mathrm{fD}}} \overline{m}_{\mathrm{fD}} \\ \left.\dfrac{\partial \overline{m}_{\mathrm{fD}}}{\partial x_{\mathrm{D}}}\right|_{x_{\mathrm{D}}=x_{1\mathrm{D}}} = -\dfrac{2\pi}{F_{\mathrm{cD}} \cdot s} \\ \overline{m}_{\mathrm{fD}}(x_{\mathrm{D}} \to \infty) = 0 \\ \left.\dfrac{\partial \overline{m}_{\mathrm{fD}}}{\partial x_{\mathrm{D}}}\right|_{x_{\mathrm{D}}=x_{2\mathrm{D}}} = 0 \\ \left.\overline{m}_{\mathrm{fD}}\right|_{x_{\mathrm{D}}=x_{2\mathrm{D}}} = 0 \end{cases} \tag{12}$$

The basic solutions of solving the above model under different boundary conditions can be as follows:

Solution of infinite boundary:

$$G(F_{\mathrm{cD}}, s, a; x_{\mathrm{D}}) = \frac{2\pi}{F_{\mathrm{cD}} \cdot s} \frac{\mathrm{e}^{a x_{1\mathrm{D}}}}{a} \mathrm{e}^{-a x_{\mathrm{D}}} \tag{13}$$

Solution of closed boundary:

$$G(F_{\mathrm{cD}}, s, a; x_{\mathrm{D}}) = -\frac{2\pi}{F_{\mathrm{cD}} \cdot s} \frac{\mathrm{e}^{a x_{1\mathrm{D}}}}{a} \left(\mathrm{e}^{a x_{\mathrm{D}}} + \mathrm{e}^{2a x_{2\mathrm{D}} - a x_{\mathrm{D}}}\right) \tag{14}$$

Solution of constant pressure boundary:

$$G(F_{\mathrm{cD}}, s, a; x_{\mathrm{D}}) = -\frac{2\pi}{F_{\mathrm{cD}} \cdot s} \frac{\mathrm{e}^{a x_{1\mathrm{D}}}}{a} \left(\mathrm{e}^{a x_{\mathrm{D}}} - \mathrm{e}^{2a x_{2\mathrm{D}} - a x_{\mathrm{D}}}\right) \tag{15}$$

with

$$a = \sqrt{\frac{s}{\eta_{\mathrm{fD}}}}$$

4.2. Coupled solution matrix

Based on the source functions in Eqs. (13)–(15), each unit in the physical model shown in Fig. 2, wellbore, cave, and fracture are discretized as illustrated in Fig. 4. Using the source function and applying flow and pressure continuity conditions across the different units, pressure equations are developed separately for the cave and the fracture. By combining these pressure equations, a coupled solution matrix is established, enabling the calculation of pressure distributions and unit flow distributions throughout the model.

Furthermore, the source function is employed to calculate the pressure resulting from the flow in cave 1, the left and right pressures due to flow in fracture region 1, the pressure from the flow in cave 2, and the left pressure due to flow in fracture region 2. The resulting equations are as follows:

$$\begin{cases} \dfrac{1}{s} - \overline{q}_{2\mathrm{D}} = s C_{\mathrm{c1D}} \overline{m}_{\mathrm{c1D}} \\ s G_{1\mathrm{l}} \overline{q}_{2\mathrm{D}} - s G_{1\mathrm{r}} \overline{q}_{3\mathrm{D}} = \overline{m}_{\mathrm{c1D}} \\ s G_{1\mathrm{r}} \overline{q}_{2\mathrm{D}} - s G_{1\mathrm{l}} \overline{q}_{3\mathrm{D}} = \overline{m}_{\mathrm{c2D}} \\ \overline{q}_{3\mathrm{D}} - \overline{q}_{4\mathrm{D}} = s C_{\mathrm{c2D}} \overline{m}_{\mathrm{c2D}} \\ s G_{2\mathrm{l}} \overline{q}_{4\mathrm{D}} = \overline{m}_{\mathrm{c2D}} \end{cases} \tag{16}$$

with

$$G_{1\mathrm{l}} = G(F_{1\mathrm{cD}}, s, a; x_{2\mathrm{D}})$$

$$G_{1\mathrm{r}} = G(F_{1\mathrm{cD}}, s, a; x_{3\mathrm{D}})$$

$$G_{2\mathrm{l}} = G(F_{2\mathrm{cD}}, s, a; x_{4\mathrm{D}})$$

The system of equations (Eq. (16)) is written in matrix form, then the coupled solution matrix is as follows:

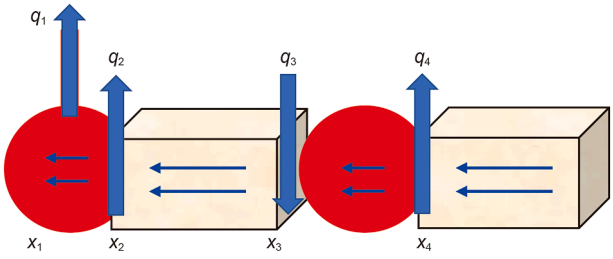

Fig. 4. Discretization and unit numbering for the W–C–F–C–F model.

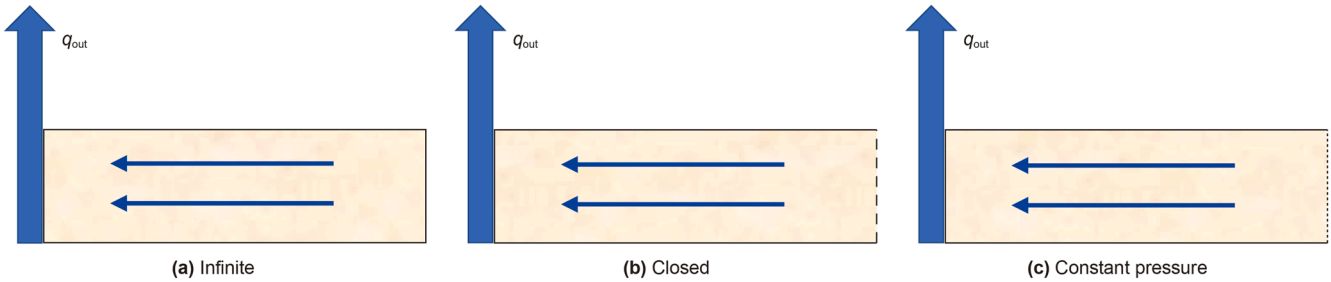

Fig. 3. Three types of boundaries.

$$\begin{bmatrix} 1 & & & sC_{c1D} & \\ sG_{1l} & -sG_{1r} & & -1 & \\ sG_{1r} & -sG_{1l} & & & -1 \\ & 1 & 1 & & -sC_{c2D} \\ & & sG_{2l} & & -1 \end{bmatrix} \cdot \begin{bmatrix} \overline{q}_{2D} \\ \overline{q}_{3D} \\ \overline{q}_{4D} \\ \overline{m}_{c1D} \\ \overline{m}_{c2D} \end{bmatrix} = \begin{bmatrix} 1/s \\ 0 \\ 0 \\ 0 \\ 0 \end{bmatrix} \tag{17}$$

Considering the wellbore and skin effects (Hegeman et al., 1993):

$$\overline{m}_{wD} = \frac{s\overline{m}_{c1D} + S}{s + C_{wD}s^2(s\overline{m}_{c1D} + S)} \tag{18}$$

Compared with traditional analytical or numerical models, our semi-analytical method employs a point-source-based coupled matrix solution that avoids case-specific derivation or grid generation. It enables fast computation for multiple wellbore–fracture–cave configurations using a unified framework. This significantly reduces the model-building and solving workload, especially compared to numerical simulations that require extensive meshing and iterative solvers.

4.3. Coupled solution matrix of different fractured-caved combinations

For different wellbore–cave–fracture combination modes, the coupled solution matrix is constructed for each unit, so that the pressure and flow distributions can be obtained. The workload of well test interpretation model establishment and solution is greatly reduced.

When the well is drilled outside the cave, the matrix of the wellbore–fracture model is as follows:

$$m_{fD} = \frac{2\pi}{F_{cD} \cdot s} \frac{1}{a} \tag{19}$$

When the well is drilled outside the cave, the matrix of the wellbore–fracture–cave–fracture model is as follows:

$$\begin{bmatrix} sG_{1l} & 0 & 1 \\ 1 & -1 & -sC_{cD} \\ 0 & sG_{2l} & -1 \end{bmatrix} \cdot \begin{bmatrix} \overline{q}_{2D} \\ \overline{q}_{3D} \\ \overline{m}_{cD} \end{bmatrix} = \begin{bmatrix} 1/s \\ 0 \\ 0 \end{bmatrix} \tag{20}$$

When the well is drilled into the cave, the matrix of the wellbore–cave–fracture model is as follows:

$$\begin{bmatrix} 1 & sC_{cD} \\ sG_{1l} & -1 \end{bmatrix} \cdot \begin{bmatrix} \overline{q}_{2D} \\ \overline{m}_{cD} \end{bmatrix} = \begin{bmatrix} 1/s \\ 0 \end{bmatrix} \tag{21}$$

By employing the Stehfest numerical inversion method (Stehfest, 1970), it is possible to obtain the bottomhole pressure solution in real space.

Compared with traditional semi-analytical models that often target single fractured-caved geometries, the proposed method adopts a modularized matrix approach, which allows flexible combination of fracture and cave elements without the need for repeated derivation. This enables relatively efficient calculations across a variety of wellbore–fracture–cave configurations encountered in fault-controlled carbonate reservoirs. While the core flow mechanisms remain consistent with classical assumptions, the extended structure enhances the model's applicability to complex reservoir systems.

4.4. Model verification

In order to verify the accuracy of these models, we choose models in the reference for analysis and verification. Pan et al. (2024) used the sequential solution method to study the pressure response characteristics of the fracture–cave model. The pressure solution of the fracture–cave models obtained by the point source solution method in this paper is compared with the pressure solution of Pan et al. (2024). The basic parameters of the model are shown in Table 3. By observing the pressure response curve shown in Fig. 5, we can find that the model in this paper is in good agreement with the curve in the reference.

To validate the flexibility and unified-treatment capability of the proposed framework, a comparison is made against the conventional approach of developing mentioned models for specific geological configurations, as exemplified by Liu (2020). In his work, Liu (2020) developed multiple, independent mathematical models to address distinct scenarios, including a “multi-fracture–cave series” model and a “fractured well communicating with a cave” model.

As shown in Fig. 6(a), by utilizing the single, unified framework proposed in this study, the typical pressure transient response of a “bead-on-a-string” configuration (e.g., a wellbore–cave–fracture–cave series) is successfully reproduced simply by inputting the dimensionless parameters ($C_{wD} = 9$, $S = 2$, $C_{c1D} = 4 \times 10^4$, $\eta_{fD} = 40$, $F_{cD} = 10$, $x_{1D} = 1$, $x_{2D} = 12$, and $C_{c2D} = 4 \times 10^5$). Similarly, Fig. 6(b) demonstrates that our model can also readily simulate the response of a fractured well communicating with a cave, by providing a different set of input parameters ($C_{wD} = 1$, $S = 2$, $C_{c1D} = 0$, $\eta_{fD} = 30$, $F_{cD} = 100$, $x_{1D} = 0$, $x_{2D} = 250$, and $C_{c2D} = 5000$).

This comparison highlights the main advantage of the proposed framework, which is that it eliminates the need for repeated mathematical re-derivation and reprogramming for each new geological scenario. Instead, users can flexibly examine a wide range of complex configurations through a modular, building-block-based configuration of elements. This helps reduce the modeling workload and improves the model's applicability.

To further demonstrate the model's practical applicability and computational performance on a real field case, we performed a history matching study of the field well data, previously presented by Pan et al. (2024).

As illustrated in Fig. 7, our model achieves a good history match with the measured pressure and pressure derivative data. The interpretation results, shown in Table 4, are in good agreement with those from the original study, validating the accuracy of our model. In terms of computational efficiency, the entire automated history matching process for this case took only 10 s on a standard workstation (Intel i7 CPU, 16 GB RAM). This quantitatively demonstrates the high efficiency of the proposed semi-analytical model for practical applications.

However, the principal advantage of our framework lies in its superior workflow efficiency when testing alternative geological concepts. For instance, evaluating a different conceptual model (e.g., a ‘well–fracture–cave’ instead of a ‘well–cave–fracture–cave’ configuration) would necessitate selecting and configuring a completely separate model within a multi-model suite like that of

Table 3
Basic parameters of the model.

Parameter	Value
Dimensionless wellbore storage coefficient C_{wD}	1
Fracture region conductivity F_{cD}	500
Dimensionless wellbore radius r_{wD}	1
Dimensionless storage coefficient of cave 2 C_{c2D}	5000
Dimensionless storage coefficient of cave 1 C_{c1D}	100
Skin factor S	0.5
Fracture hydraulic diffusivity η_{fD}	50

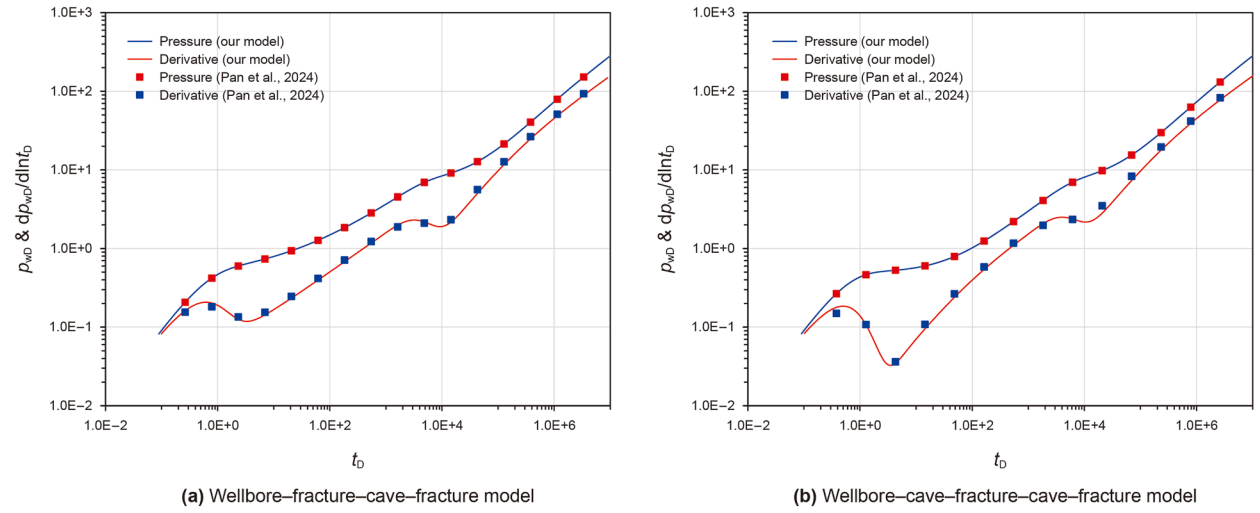

(a) Wellbore–fracture–cave–fracture model **(b)** Wellbore–cave–fracture–cave–fracture model

Fig. 5. Model verification results.

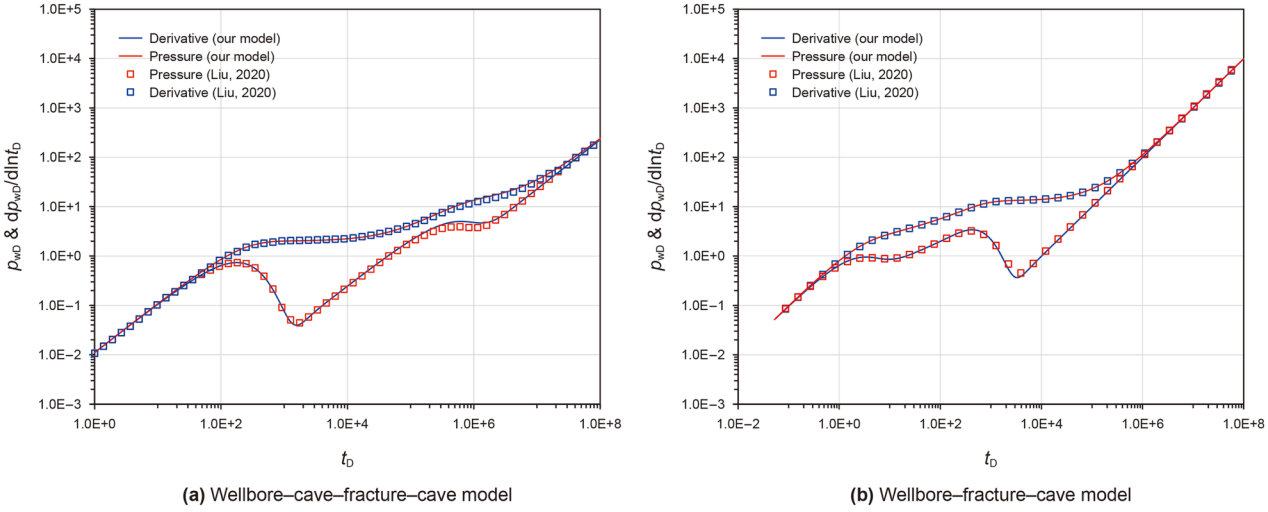

(a) Wellbore–cave–fracture–cave model **(b)** Wellbore–fracture–cave model

Fig. 6. Validation of the unified framework by reproducing typical pressure transient responses for distinct geological configurations.

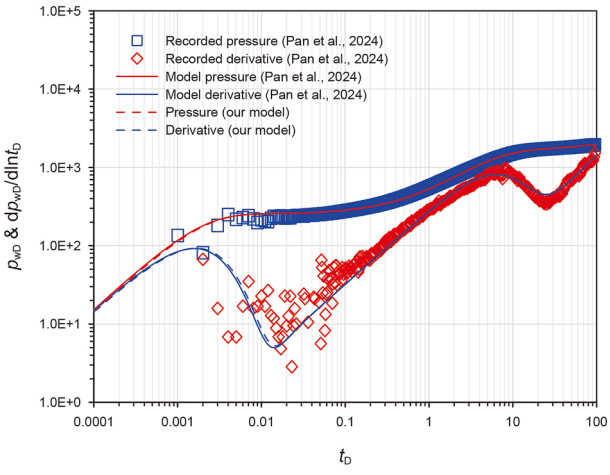

Fig. 7. History matching of the field case from Pan et al. (2024).

Pan et al. (2024). In contrast, our unified framework requires only a minor modification to the input connectivity matrix. This ability to rapidly and seamlessly test multiple hypotheses is a key practical advantage that significantly reduces the overall modeling workload and enhances the iterative interpretation process.

5. Pressure response characteristics

5.1. Type curves of typical fracture–cave combination models

To analyze the fluid flow characteristics of different fracture–cave combination models, the pressure and pressure derivative curves under various fracture–cave distributions are examined by plotting the pressure response curves on double logarithmic coordinates. Fig. 8(e) and (f) illustrate two complex reservoir configurations that incorporate acid-fractured (AF) well completions. In these models, acid fracturing is used to enhance the conductivity near the wellbore, followed by a sequence of fracture–cave structures. Specifically, the W–AF–C–F–C–F model represents a scenario where the acid fracturing treatment fully penetrates and enhances the entire fracture region. In contrast, the W–AF–F–C–F–C–F model reflects a partial stimulation case, where the acid fracturing only modifies the near-wellbore

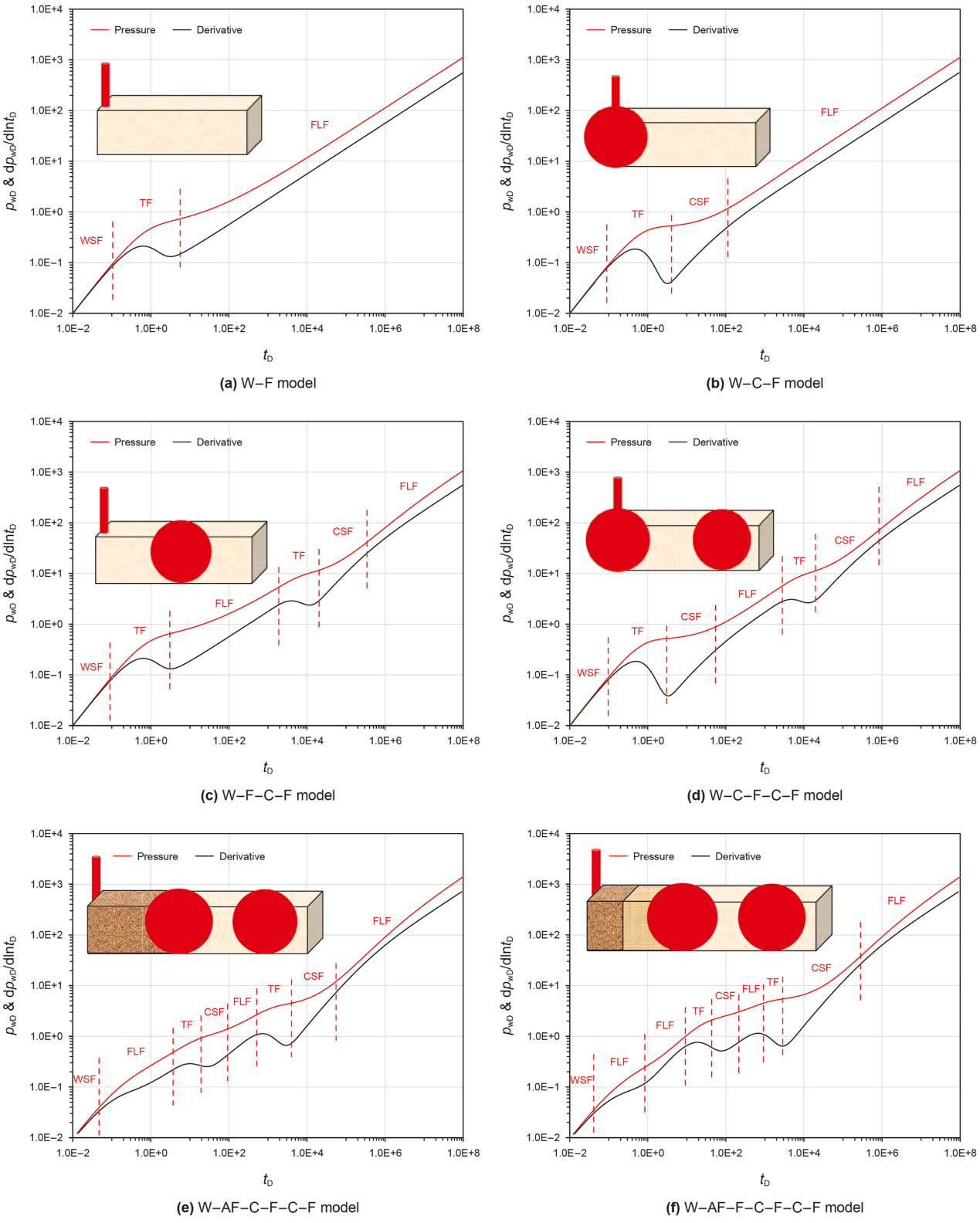

Fig. 8. Pressure response curves under different wellbore–cave–fracture combination models (notes: W-wellbore; AF-acid fracture; C-cave; F-fracture region).

segment, while the downstream sections remain as natural fracture regions. The basic parameters for this model are provided in Table 5. For the acid-fractured models in Fig. 8(e) and (f), specific fracture parameters are modified. In Fig. 8(e), the dimensionless fracture lengths are 20, 200, and 300, with conductivities of 200 and 50 for the first two regions, respectively. In Fig. 8(f), the dimensionless fracture lengths are 10, 20, 200, and 300, and the first two regions have a conductivity of 200. A uniform skin factor of 0.1 is applied in both cases, while other parameters remain consistent with Table 5.

Table 4
Comparison of interpretation results between this work and Pan et al. (2024).

Model	Wellbore storage coefficient, m^3/MPa	Skin factor	Cave 1 volume, 10^4 m^3	Fracture region permeability, μm^2	Cave 2 volume, 10^4 m^3
Pan et al. (2024)	0.29	5.87	1.19	0.482	12.10
Our model	0.31	5.92	1.08	0.480	12.02

Table 5
Basic parameters of the model.

Parameter	Value
Dimensionless wellbore storage coefficient C_{wD}	1
Fracture region conductivity F_{cD}	400
Dimensionless wellbore radius r_{wD}	1
Dimensionless storage coefficient of cave 1 C_{c1D}	80
Dimensionless storage coefficient of cave 2 C_{c2D}	5000
Skin factor S	0.5
Dimensionless fracture hydraulic diffusivity η_{fD}	40
Dimensionless fracture region 1 length x_{fD}	600

The pressure response charts of the wellbore–fracture model, wellbore–cave–fracture model, wellbore–fracture–cave–fracture model, wellbore–cave–fracture–cave–fracture model, wellbore–acid fracture–cave–fracture–cave–fracture model, and wellbore-acid fracture–fracture–cave–fracture–cave–fracture model are analyzed.

As shown in Fig. 8, according to the six types of typical curves, the following four main stages are divided: constant wellbore storage flow stage, fracture region linear flow stage, karst cave storage flow stage, and transition flow stage.

(1) Wellbore storage flow stage (WSF): The wellbore is single-phase gas, and the wellbore storage capacity is determined by the gas compression coefficient. The pressure curve and pressure derivative curve of this stage overlap and are straight line segments with a slope of 1.
(2) Fracture region linear flow stage (FLF): According to the basic assumptions, the flow in the fracture region conforms to Darcy's law, which is presented as one-dimensional linear flow. On the pressure derivative curve, it appears as a straight-line segment with a slope of 1/2.
(3) Cave storage flow stage (CSF): The flow form in the large-scale cave is free flow, and the pressure derivative curve in this stage is a straight-line segment with a slope of 1.
(4) Transition flow stage (TF): Transition flow is the intermediate flow stage in the transition process of the wellbore, fracture region, and cave flow stage.

Among them, the flow stages of the wellbore–fracture model are constant wellbore storage flow, transition flow, and fracture region linear flow. The flow stages of the wellbore–cave–fracture model are constant wellbore storage flow, transition flow, cave storage flow, transition flow, and fracture region linear flow. The flow stages of the wellbore–fracture–cave–fracture model are constant wellbore storage flow, transition flow, linear flow in the fracture region, transition flow, cave storage flow, transition flow, and linear flow in the fracture region. The flow stages of the wellbore–cave–fracture–cave-fracture model are constant wellbore storage flow, transition flow, cave storage flow, transition flow, fracture region linear flow, transition flow, cave storage flow, transition flow, and fracture region linear flow. The flow stages of the wellbore–acid fracture–cave–fracture–cave–fracture model are constant wellbore storage flow, fracture region linear flow, transition flow, cave storage flow, transition flow, fracture region linear flow, transition flow, cave storage flow, and fracture region linear flow. The flow stages of the wellbore–acid fracture–fracture–cave–fracture–cave–fracture model are constant wellbore storage flow, fracture region linear flow, fracture region linear flow, transition flow, cave storage flow, transition flow, fracture region linear flow, transition flow, cave storage flow, and fracture region linear flow.

5.2. Effect of pressure response of the wellbore–fracture model

The effect of skin factor and fracture region conductivity on the pressure response curves are analyzed by the wellbore–fracture model, as shown in Figs. 9 and 10.

Skin factor: By setting different skin factor values (S = 0.1, 0.5, 2.5), it is found that the skin factor affects the end time of the wellbore storage flow. The larger the skin factor, the greater the flow resistance near the bottom of the well, the longer the storage

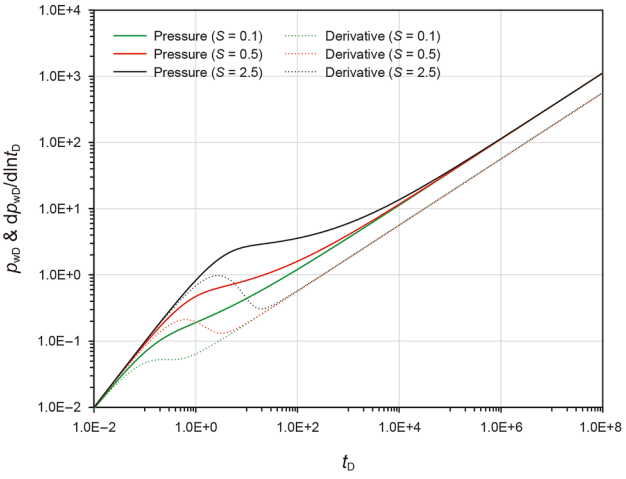

Fig. 9. Sensitivity analysis under different skin factors.

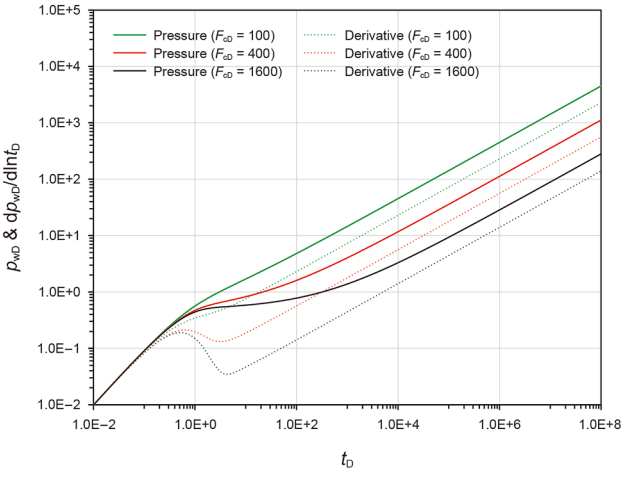

Fig. 10. Sensitivity analysis under different fracture region conductivities.

flow time, and the shallower the concave at the initial stage of flow.

The conductivity of fracture region: By setting different fracture region conductivity values (F_{cD} = 100, 400, 1600), it is found that the conductivity of the fracture region affects the occurrence of the storage flow section and the level of linear flow section on the pressure response curve. The greater the conductivity of the fracture region, the faster the pressure propagation, and the more obvious the storage effect from the fracture region to the wellbore.

5.3. Effect of pressure response of the wellbore–fracture–cave–fracture model

The sensitivity analysis of fracture region length and fracture region width to pressure response curve is carried out using the wellbore–fracture–cave–fracture model, as shown in Figs. 11 and 12.

Fracture region length: By setting different fracture region length values (x_{fD} = 300, 600, 900), it is found that the length of the fracture region affects the duration of linear flow. The longer the fracture region is, the longer the duration of linear flow is, and the concave on the pressure derivative curve moves upward.

Fracture region width: By setting different fracture region conductivity to represent the change of fracture region width (F_{cD} = 100, 400, 1600), it is found that the fracture region width affects the start time of linear flow. The wider the fracture region is, the earlier the start time of linear flow is. The concave on the pressure derivative curve moves downward.

5.4. Effect of pressure response of wellbore–cave–fracture–cave–fracture model

The sensitivity analysis of cave volume to pressure response curve is carried out by using the wellbore–cave–fracture–cave–fracture model, as shown in Figs. 13 and 14.

Cave 1 volume: By setting different cave storage coefficients to represent different cave volumes (C_{c1D} = 20, 80, 320), it is found that the volume of cave 1 affects the depth of the first concave and affects the time to enter the next flow stage. The larger the volume of cave 1 is, the longer the time required for the pressure wave to propagate to the next stage is, and the stronger the ability to supply to the next flow stage is. The larger the volume of cave 1 is, the wider and deeper the concave is, and the slope of the pressure derivative curve is closer to 1.

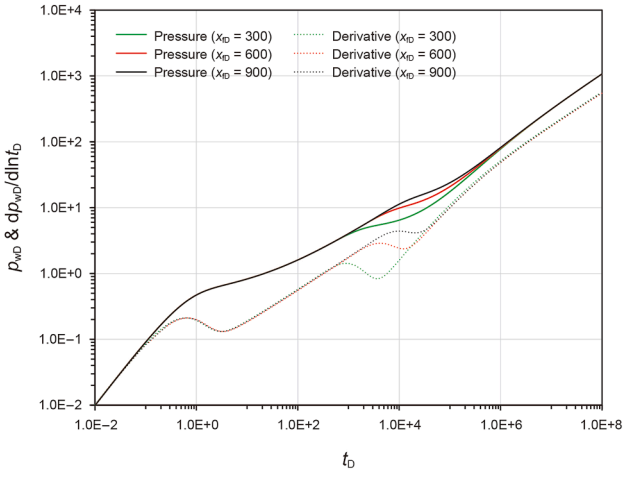

Fig. 11. Sensitivity analysis under different fracture region lengths.

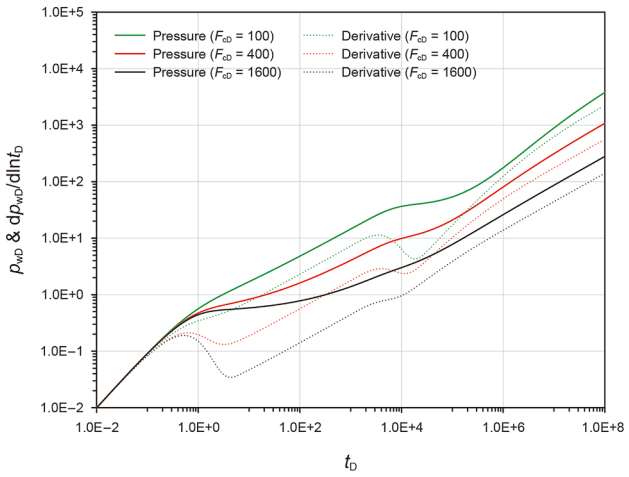

Fig. 12. Sensitivity analysis under different fracture region widths.

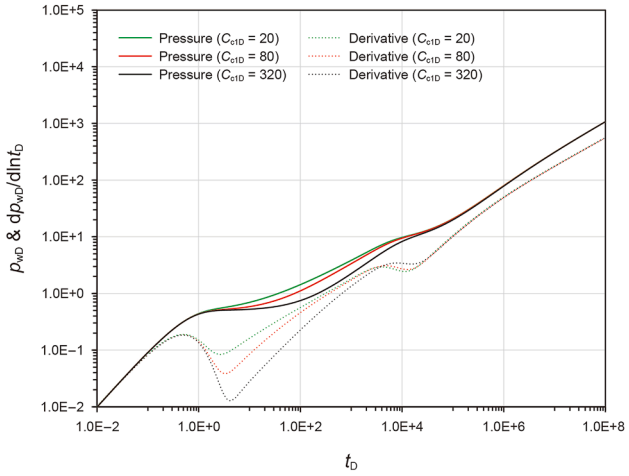

Fig. 13. Sensitivity analysis under different cave 1 volumes.

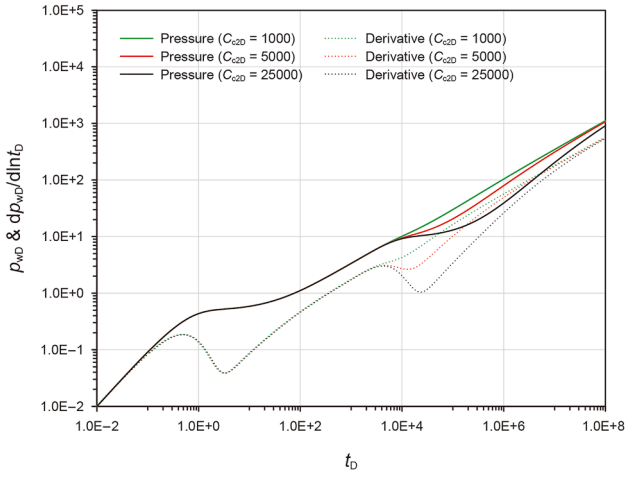

Fig. 14. Sensitivity analysis of different cave 2 volumes.

Cave 2 volume: By setting different cave 2 storage coefficient values (C_{c2D} = 1000, 5000, 25000), it is found that the cave 2 volume affects the depth of the second concave. The larger the cave 2 volume is, the stronger the supply capacity to the next flow stage

is, and the wider and deeper the concave is. Moreover, the volume change of the far side cave (cave 2) has no obvious effect on the flow of the near-wellbore cave (cave 1).

6. Case study

To evaluate the applicability of the proposed model under different geological configurations, three representative scenarios are examined in this section, including a wellbore–fracture model, a wellbore–fracture–cave model, and a wellbore–cave–fracture–cave model. Each case incorporates both the qualitative identification of typical flow regimes and the quantitative interpretation of key parameters, enabling a comprehensive understanding of pressure behaviors and geological implications. Standard preprocessing was applied to the field data to enhance derivative stability while retaining essential flow regime features.

6.1. Wellbore–fracture model

6.1.1. Typical feature analysis and qualitative interpretation

The pressure derivative curve exhibits a linear flow stage in the fracture region. The late-time upward trend suggests potential boundary effects and may also imply the presence of a secondary fracture region connected to the far end of the reservoir. Figs. 15 and 16 present the production and pressure history, along with the fitting results from the well test interpretation. As shown in Fig. 16(a), the flow stages can be divided into wellbore storage, transition flow, fracture linear flow, and boundary response.

6.1.2. Parameter interpretation

Based on the flow stage analysis of the reservoir, the established well test interpretation model is used. The results of well test interpretation and analysis of well A are shown in Table 6, in which the well storage coefficient is 0.16 m^3/MPa, the skin factor is 5.41, the permeability of the fracture region is 0.06 μm^2, the length of the fracture region is 712.54 m.

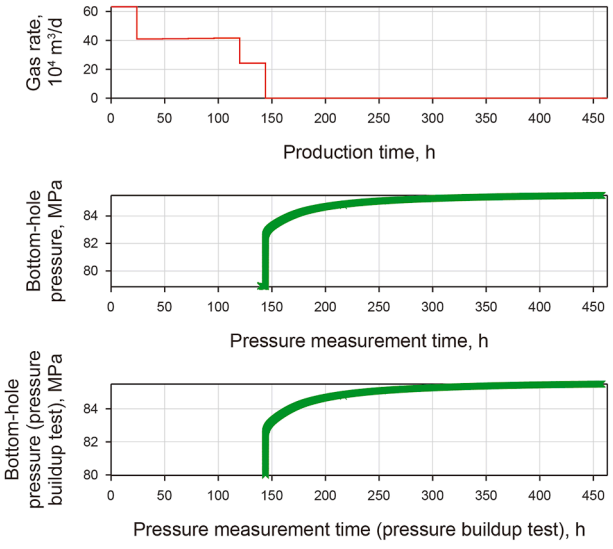

Fig. 15. Production history and pressure of well A.

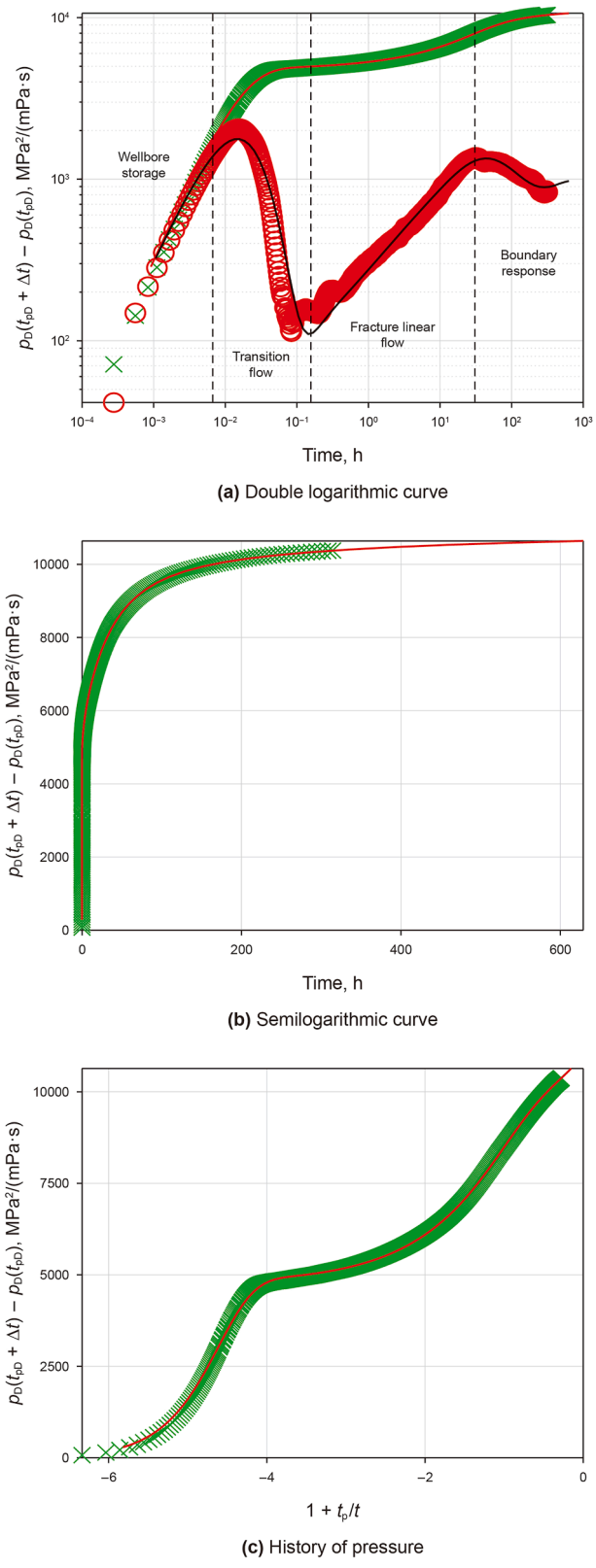

Fig. 16. Well test interpretation fitting results of well A (t_p is the production time; t is the shut-in time).

Table 6
Well test interpretation analysis results of well A.

Medium	Wellbore		Fracture region	
Parameter	Wellbore storage coefficient, m^3/MPa	Skin factor	Fracture region permeability, μm^2	Fracture region length, m
Value	0.16	5.41	0.06	712.54

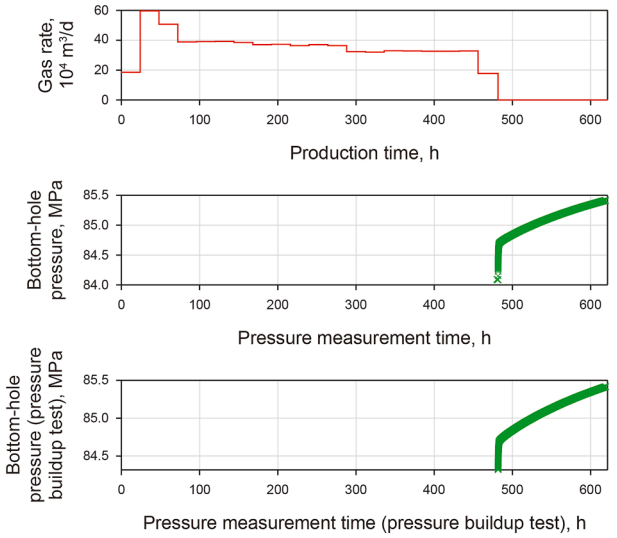

Fig. 17. Production history and pressure of well B.

6.2. Wellbore–fracture–cave model

6.2.1. Typical feature analysis and qualitative interpretation

The pressure derivative on the pressure recovery curve of the well consists of one linear section, with a concave section after. The flow stages include the linear flow section of the fracture region, the storage flow section of the cave. Figs. 17 and 18 present the production and pressure history, along with the fitting results from the well test interpretation. As shown in Fig. 18(a), the log-log derivative curve reveals five flow stages: wellbore storage, transition flow, fracture linear flow, transition flow, and cave storage.

6.2.2. Parameter interpretation

Based on the flow stage analysis of the reservoir, the established well test interpretation model is used. The results of well test interpretation and analysis of well B are shown in Table 7, in which the well storage coefficient is 2.92 m^3/MPa, the skin factor is 1.68, the permeability of the fracture region is 0.03 μm^2, the length of the fracture region is 23.62 m, and the volume of the cave is 12.8×10^4 m^3. The well is drilled on the fracture region, and the distance between the well and the cave is close.

6.3. Wellbore–cave–fracture–cave model

6.3.1. Typical feature analysis and qualitative interpretation

The pressure derivative in the pressure recovery curve of the well displays two concave sections with a linear section in the middle. These features reveal the flow stages, which include the

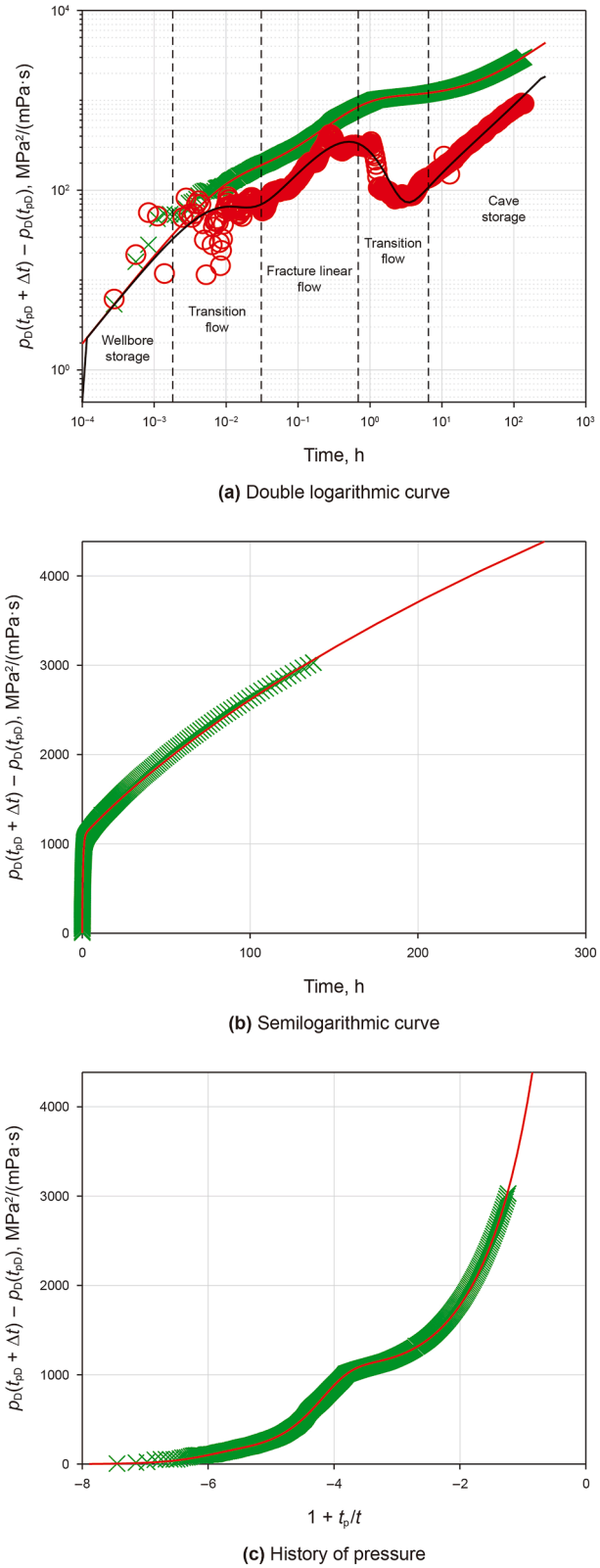

Fig. 18. Well test interpretation fitting results of well B.

Table 7
Well test interpretation analysis results of well B.

Medium	Wellbore		Fracture region		Cave
Parameter	Wellbore storage coefficient, m^3/MPa	Skin factor	Fracture region permeability, μm^2	Fracture region length, m	Volume, 10^4 m^3
Value	2.92	1.68	0.03	23.62	12.8

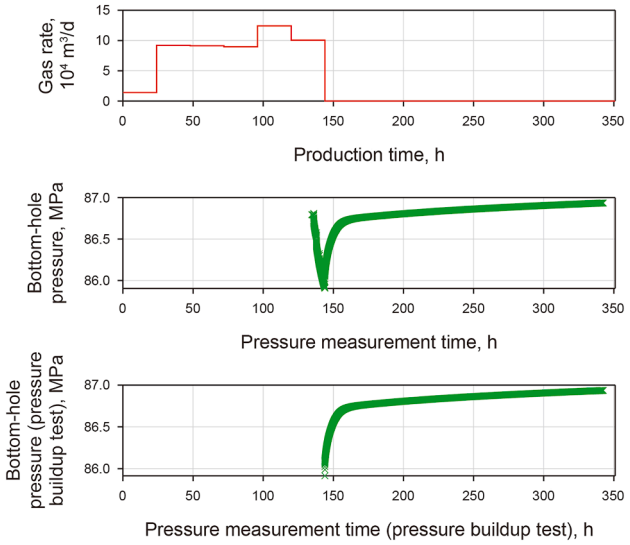

Fig. 19. Production history and pressure of well C.

cave 1 storage flow section, the fracture region linear flow section, and the cave 2 storage flow section. Figs. 19 and 20 present the production and pressure history, along with the fitting results from the well test interpretation. As shown in Fig. 20(a), the pressure derivative curve can be divided into six flow stages: wellbore storage, transition flow, cave 1 storage, fracture linear flow, transition flow, and cave 2 storage.

6.3.2. *Parameter interpretation*

Based on the flow stage analysis of the reservoir, the established well test interpretation model is used. The well test interpretation and analysis results for well C are summarized in Table 8, in which the well storage coefficient is 2.16 m^3/MPa, the skin factor is 0.6863, the permeability of the fracture region is 0.52 μm^2, the length of the fracture region is 245.98 m, the volume of cave 1 is 6.53 × 10^4 m^3, and the volume of cave 2 is 39.4 × 10^4 m^3.

7. Conclusions

This study introduces a novel well test interpretation model and an efficient semi-analytical solution method for fault-controlled fractured-caved reservoirs with typical fracture–cave combinations. By integrating fluid flow and storage flow theories, the study systematically investigates the effect of various reservoir parameters on the pressure response characteristics of fault-controlled fractured–caved reservoirs. Field applications of the proposed models led to the following findings:

(1) Mathematical models for fluid flow in the fracture region were developed, incorporating source-sink terms. The source functions were derived to account for different boundary conditions, including various karst and wellbore boundaries. The proposed model is applicable to the diverse boundary conditions encountered in the fracture region.
(2) A generalized well test interpretation model was developed, suitable for a wide range of well, fracture region, and cave

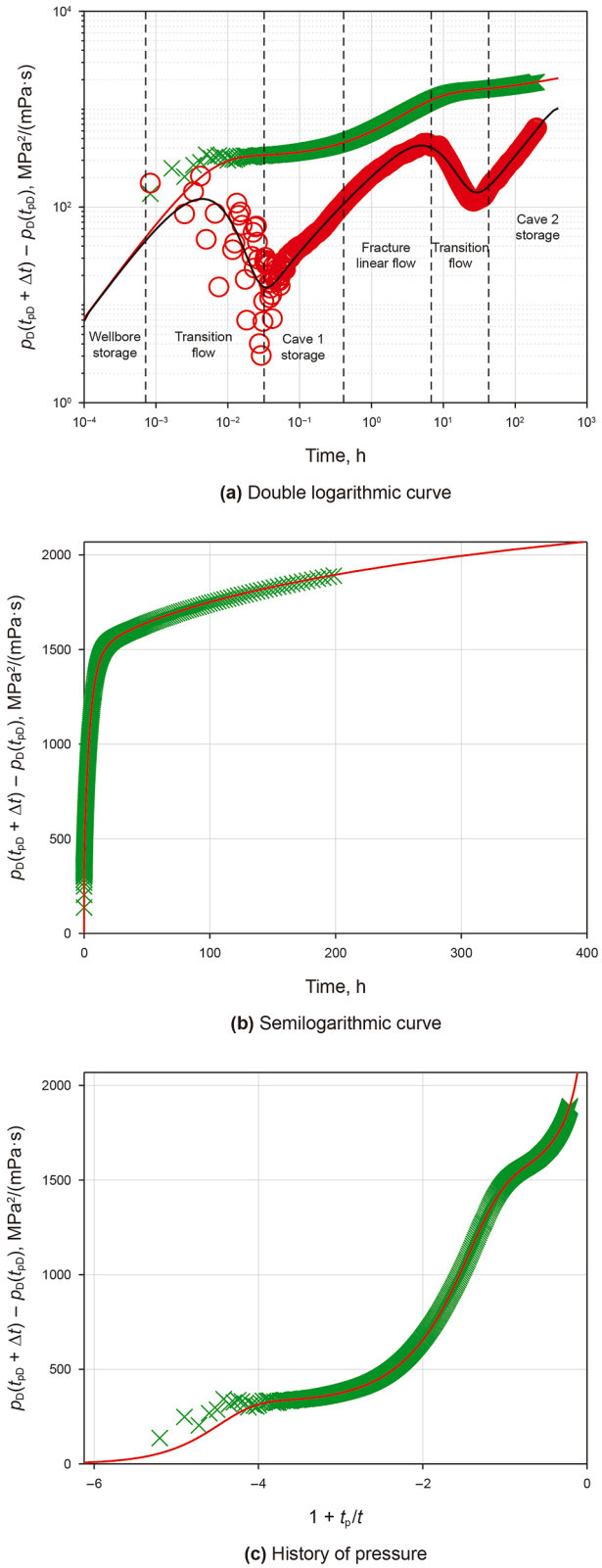

Fig. 20. Well test interpretation fitting results of well C.

Table 8
Well test interpretation analysis results of well C.

Medium	Wellbore		Cave	Fracture region		Cave
Parameter	Wellbore storage coefficient, m^3/MPa	Skin factor	Volume, 10^4 m^3	Fracture region permeability, μm^2	Fracture region length, m	Volume, 10^4 m^3
Value	2.16	0.6863	6.53	0.52	245.98	39.4

combinations. The bottom-hole pressure solution was derived through matrix computation, enabling the construction of a coupled solution matrix for individual units. This approach allows for the determination of pressure and flow distributions without the need for a separate well test model for each physical configuration. Consequently, this method reduces modeling effort while enhancing the flexibility of well test models.

(3) The storage and skin effects significantly affect the early stage of fluid flow. A larger storage coefficient results in a smaller intercept with the *y*-axis. The skin factor affects the wellbore flow termination time, with a higher skin factor leading to a longer wellbore flow duration. The length and conductivity of fracture regions strongly affect the linear flow within the fracture regions. The length of the fracture regions affects the duration of linear flow, while the conductivity impacts the start of linear flow, with higher permeability leading to faster pressure propagation and an earlier onset of linear flow. The cave volume plays a crucial role in cave storage flow, with a larger cave volume corresponding to a greater supply capacity and a wider, deeper concave shape.

(4) The pressure recovery data of three representative wellbore–fracture–cave combinations from the Shunbei fracture–cave gas reservoir was effectively interpreted using the established well test interpretation models. This enables the precise determination of wellbore, fracture region, and cave parameters, providing valuable insights for the development of fault-controlled fractured-caved reservoirs.

CRediT authorship contribution statement

Pin Jia: Conceptualization, Data curation, Methodology, Writing – original draft. **Quan-Yu Pan:** Formal analysis, Methodology, Writing – review & editing. **Jia Li:** Investigation, Visualization. **Jiang-Peng Hu:** Formal analysis, Visualization. **Yu-Cheng Wu:** Investigation, Validation. **Lin-Song Cheng:** Supervision, Writing – review & editing.

Data availability

The data that support the findings of this study are available from the corresponding author upon reasonable request.

Declaration of competing interest

The authors declare that they have no known competing financial interests or personal relationships that could have appeared to influence the work reported in this paper.

Acknowledgments

The authors express their gratitude to Shunbei field for providing the seismic response curves and raw data. Additionally, the authors acknowledge that this study was partially supported by the National Natural Science Foundation of China Project (No. 52474057).

Appendix A. Mathematical modeling of flow in fracture–cave models

In Appendix A, we list the development of mathematical models for flow in wellbore–cave–fracture–cave–fracture model.

According to the expression of gas compressibility, the transformations of Eqs. (1)–(3), (6), and (7) are as follows:

$$\frac{1}{B_g}=\frac{p}{ZT}\frac{Z_{sc}T_{sc}}{p_{sc}} \tag{A.1}$$

$$q_{sfg}-q_{scg}=24V_bc_g\frac{Z_{sc}T_{sc}\mu_g}{p_{sc}T}\frac{p}{Z\mu_g}\frac{dp_w}{dt} \tag{A.2}$$

$$q_{sfg}=-24V_{c1}\phi_{c1}c_g\frac{Z_{sc}T_{sc}\mu_g}{p_{sc}T}\frac{p}{Z\mu_g}\frac{dp_{c1}}{dt} -86.4k_{f1}w_{f1}h\frac{Z_{sc}T_{sc}}{p_{sc}T}\frac{p}{Z\mu_g}\frac{\partial p_{f1}}{\partial x}\Big|_{x=x_1} \tag{A.3}$$

$$\frac{1}{\partial x}\left(\frac{p_{f1}}{Z\mu_g}\frac{\partial p_{f1}}{\partial x}\right)=\frac{\phi_{f1}c_g\mu_g}{k_{f1}}\left(\frac{p_{f1}}{Z\mu_g}\frac{\partial p_{f1}}{\partial t}\right) \tag{A.4}$$

$$86.4k_{f1}w_{f1}h\frac{Z_{sc}T_{sc}}{p_{sc}T}\frac{p}{Z\mu_g}\frac{\partial p_{f1}}{\partial x}\Big|_{x=x_2}=-24V_{c2}\phi_{c2}c_g\frac{Z_{sc}T_{sc}\mu_g}{p_{sc}T}\frac{p}{Z\mu_g}\frac{dp_{c2}}{dt} -86.4k_{f2}w_{f2}h\frac{Z_{sc}T_{sc}}{p_{sc}T}\frac{p}{Z\mu_g}\frac{\partial p_{f2}}{\partial x}\Big|_{x=x_3}$$

$$\frac{1}{\partial x}\left(\frac{p_{f2}}{Z\mu_g}\frac{\partial p_{f2}}{\partial x}\right)=\frac{\phi_{f2}c_g\mu_g}{k_{f2}}\left(\frac{p_{f2}}{Z\mu_g}\frac{\partial p_{f2}}{\partial t}\right) \tag{A.5}$$

Introducing gas pseudo-pressure, there are

$$m(p)=2\int_{p_0}^{p}\frac{p}{Z\mu}dp \tag{A.6}$$

$$q_{sfg}-q_{scg}=24V_bc_g\frac{Z_{sc}T_{sc}\mu_g}{p_{sc}T}\frac{dm_w}{dt} \tag{A.7}$$

$$q_{sfg}=-24V_{c1}\phi_{c1}c_g\frac{Z_{sc}T_{sc}\mu_g}{p_{sc}T}\frac{dm_{c1}}{dt} -86.4k_{f1}w_{f1}h\frac{Z_{sc}T_{sc}}{p_{sc}T}\frac{\partial m_{f1}}{\partial x}\Big|_{x=x_1} \tag{A.8}$$

$$\frac{1}{\partial x}\left(\frac{\partial m_{f1}}{\partial x}\right)=\frac{\phi_{f1}c_g\mu_g}{k_{f1}}\left(\frac{\partial m_{f1}}{\partial t}\right) \tag{A.9}$$

$$86.4k_{f1}w_{f1}h\frac{Z_{sc}T_{sc}}{p_{sc}T}\frac{\partial m_{f1}}{\partial x}\bigg|_{x=x_2} = -24V_{c2}\phi_{c2}c_g\frac{Z_{sc}T_{sc}\mu_g}{p_{sc}T}\frac{dm_{c2}}{dt} - 86.4k_{f2}w_{f2}h\frac{Z_{sc}T_{sc}}{p_{sc}T}\frac{\partial m_{f2}}{\partial x}\bigg|_{x=x_3}$$

$$\frac{1}{\partial x}\left(\frac{\partial m_{f2}}{\partial x}\right) = \frac{\phi_{f2}c_g\mu_g}{k_{f2}}\left(\frac{\partial m_{f2}}{\partial t}\right) \tag{A.10}$$

The following are the definitions of dimensionless pressure, dimensionless time and other variables:

$$m_D = \frac{78.489k_rh[m(p_i)-m(p)]}{q_{scg}T} \tag{A.11}$$

$$m_D = \frac{78.489k_rh[m(p_i)-m(p)]}{q_{scg}T} \tag{A.12}$$

$$t_D = \frac{3.6k_rt}{\phi_r\mu_rc_{tr}r_w^2} \tag{A.13}$$

$$\eta_{fD} = \frac{k_f}{\phi_f\mu_gc_g}\frac{\phi_r\mu_gc_{tr}}{k_r} \tag{A.14}$$

$$F_{cD} = \frac{k_fw_f}{k_rr_w} \tag{A.15}$$

$$C_{cD} = \frac{V_c\phi_cc_g}{2\pi\phi_rc_{tr}hr_w^2} \tag{A.16}$$

The dimensionless form of Eqs. (1)–(9) can be obtained as follows:

$$\begin{cases} 2\pi q_{sfgD} = 2\pi C_{c1D}\dfrac{dm_{v1D}}{dt_D} + F_{c1D}\left(\dfrac{\partial m_{f1D}}{\partial x_D}\right)_{x_D=x_{1D}} \\ \dfrac{\partial^2 m_{f1D}}{\partial x^2} = \dfrac{1}{\eta_{f1D}}\dfrac{\partial m_{f1D}}{\partial t_D} \\ F_{c1D}\left(\dfrac{\partial m_{f1D}}{\partial x_D}\right)_{x_D=x_{2D}} = -2\pi C_{c2D}\dfrac{dm_{c2D}}{dt_D} - F_{c2D}\left(\dfrac{\partial m_{f2D}}{\partial x_D}\right)_{x_D=x_{3D}} \\ \dfrac{\partial^2 m_{f2D}}{\partial x^2} = \dfrac{1}{\eta_{f2D}}\dfrac{\partial m_{f2D}}{\partial t_D} \\ 1 - q_{sfgD} = 2\pi C_{wD}\dfrac{dm_{wD}}{dt_D} \\ m_{c1D} = m_{f1D}(x_D,0) = m_{c2D} = m_{f2D}(x_D,0) = 0 \\ m_{f1D}\big|_{x_D=x_{1D}} = m_{c1D} \\ m_{f1D}\big|_{x_D=x_{2D}} = m_{c2D} \\ m_{f2D}\big|_{x_D=x_{3D}} = m_{c2D} \\ m_{f2D}\big|_{x_D\to\infty} = 0 \\ m_{f2D}\big|_{x_D=x_{4D}} = 0 \\ \dfrac{\partial m_{f2D}}{\partial x_D}\bigg|_{x_D=x_{4D}} = 0 \end{cases} \tag{A.17}$$

After Laplace transformation of Eqs. (1)–(9), there are

$$\begin{cases} 2\pi\overline{q}_{\mathrm{sfgD}} = 2\pi s C_{\mathrm{c1D}}\overline{m}_{\mathrm{c1D}} + F_{\mathrm{c1D}}\left(\dfrac{\partial\overline{m}_{\mathrm{f1D}}}{\partial x_{\mathrm{D}}}\right)_{x_{\mathrm{D}}=x_{1\mathrm{D}}} \\ \dfrac{\partial^2 m_{\mathrm{f1D}}}{\partial x^2} = \dfrac{s}{\eta_{\mathrm{f1D}}}\overline{m}_{\mathrm{f1D}} \\ F_{\mathrm{c1D}}\left(\dfrac{\partial\overline{m}_{\mathrm{f1D}}}{\partial x_{\mathrm{D}}}\right)_{x_{\mathrm{D}}=x_{2\mathrm{D}}} = -2\pi s C_{\mathrm{c2D}}\overline{m}_{\mathrm{c2D}} - F_{\mathrm{c2D}}\left(\dfrac{\partial\overline{m}_{\mathrm{f2D}}}{\partial x_{\mathrm{D}}}\right)_{x_{\mathrm{D}}=x_{3\mathrm{D}}} \\ \dfrac{\partial^2\overline{m}_{\mathrm{f2D}}}{\partial x^2} = \dfrac{s}{\eta_{\mathrm{f2D}}}\overline{m}_{\mathrm{f2D}} \\ \dfrac{1}{s} - \overline{q}_{\mathrm{sfgD}} = 2\pi s C_{\mathrm{wD}}\overline{m}_{\mathrm{wD}} \\ \overline{m}_{\mathrm{f1D}}\big|_{x_{\mathrm{D}}=x_{1\mathrm{D}}} = \overline{m}_{\mathrm{c1D}} \\ \overline{m}_{\mathrm{f1D}}\big|_{x_{\mathrm{D}}=x_{2\mathrm{D}}} = \overline{m}_{\mathrm{c2D}} \\ \overline{m}_{\mathrm{f2D}}\big|_{x_{\mathrm{D}}=x_{3\mathrm{D}}} = \overline{m}_{\mathrm{c2D}} \\ \overline{m}_{\mathrm{f2D}}\big|_{x_{\mathrm{D}}\to\infty} = 0 \\ \overline{m}_{\mathrm{f2D}}\big|_{x_{\mathrm{D}}=x_{4\mathrm{D}}} = 0 \\ \dfrac{\partial\overline{m}_{\mathrm{f2D}}}{\partial x_{\mathrm{D}}}\Big|_{x_{\mathrm{D}}=x_{4\mathrm{D}}} = 0 \end{cases} \tag{A.18}$$

Appendix B. Source function solutions for fracture region flow

According to the flow equation in Eq. (12):

$$\frac{\partial^2\overline{m}_{\mathrm{fD}}}{\partial x_{\mathrm{D}}^2} = \frac{s}{\eta_{\mathrm{fD}}}\overline{m}_{\mathrm{fD}} \tag{B.1}$$

First, the generalized solution of the equation is obtained

$$\overline{m}_{\mathrm{fD}}(x_{\mathrm{D}}) = C_1 e^{ax_{\mathrm{D}}} + C_2 e^{-ax_{\mathrm{D}}} \tag{B.2}$$

with

$$a = \sqrt{\frac{s}{\eta_{\mathrm{fD}}}}$$

(1) According to the infinite boundary condition:

$$\overline{m}_{\mathrm{fD}}(x_{\mathrm{D}} \to +\infty) = 0 \tag{B.3}$$

Therefore

$$C_1 = 0$$

$$\overline{m}_{\mathrm{fD}}(x_{\mathrm{D}}) = C_2 e^{-ax_{\mathrm{D}}} \tag{B.4}$$

Moreover, according to the constant production boundary conditions:

$$\frac{\partial\overline{m}_{\mathrm{fD}}}{\partial x_{\mathrm{D}}}\Big|_{x_{\mathrm{D}}=x_{1\mathrm{D}}} = -\frac{2\pi}{F_{\mathrm{cD}}\cdot s} \tag{B.5}$$

Therefore,

$$C_2 e^{-ax_{1\mathrm{D}}}\cdot(-a) = -\frac{2\pi}{F_{\mathrm{cD}}\cdot s} \tag{B.6}$$

$$C_2 = \frac{2\pi}{F_{\mathrm{cD}}\cdot s}\frac{e^{ax_{1\mathrm{D}}}}{a} \tag{B.7}$$

Thus, the fracture region pressure solution at the infinite boundary is

$$\overline{m}_{\mathrm{fD}}(x_{\mathrm{D}}) = \frac{2\pi}{F_{\mathrm{cD}}\cdot s}\frac{e^{ax_{1\mathrm{D}}}}{a}e^{-ax_{\mathrm{D}}} \tag{B.8}$$

(2) According to the closed boundary conditions:

$$\frac{\partial\overline{m}_{\mathrm{fD}}}{\partial x_{\mathrm{D}}}\Big|_{x_{\mathrm{D}}=x_{2\mathrm{D}}} = 0 \tag{B.9}$$

Combining Eq. (B.9) with the inner boundary conditions gives

$$\begin{cases} C_1 e^{ax_{1\mathrm{D}}}\cdot a - C_2 e^{-ax_{1\mathrm{D}}}\cdot a = -\dfrac{2\pi}{F_{\mathrm{cD}}\cdot s} \\ C_1 e^{ax_{2\mathrm{D}}}\cdot a - C_2 e^{-ax_{2\mathrm{D}}}\cdot a = 0 \end{cases} \tag{B.10}$$

Therefore,

$$\begin{cases} C_1 = -\dfrac{2\pi}{F_{\mathrm{cD}}\cdot s}\dfrac{e^{ax_{1\mathrm{D}}}}{a} \\ C_2 = -\dfrac{2\pi}{F_{\mathrm{cD}}\cdot s}\dfrac{e^{ax_{1\mathrm{D}}}}{a}e^{2ax_{2\mathrm{D}}} \end{cases} \tag{B.11}$$

Thus, the fracture region pressure solution at the closed boundary conditions is

$$\overline{m}_{\mathrm{fD}}(x_{\mathrm{D}}) = -\frac{2\pi}{F_{\mathrm{cD}}\cdot s}\frac{e^{ax_{1\mathrm{D}}}}{a}\left(e^{ax_{\mathrm{D}}} + e^{2ax_{2\mathrm{D}}-ax_{\mathrm{D}}}\right) \tag{B.12}$$

(3) According to the constant-pressure boundary condition:

$$\overline{m}_{\mathrm{fD}}(x_{\mathrm{D}} = x_{2\mathrm{D}}) = 0 \tag{B.13}$$

Combining Eq. (B.13) with the inner boundary conditions gives:

$$\begin{cases} C_1 e^{ax_{1\mathrm{D}}}\cdot a - C_2 e^{-ax_{1\mathrm{D}}}\cdot a = -\dfrac{2\pi}{F_{\mathrm{cD}}\cdot s} \\ C_1 e^{ax_{2\mathrm{D}}}\cdot a + C_2 e^{-ax_{2\mathrm{D}}} = 0 \end{cases} \tag{B.14}$$

Therefore,

$$\begin{cases} C_1 = -\dfrac{2\pi}{F_{\mathrm{cD}}\cdot s}\dfrac{e^{ax_{1\mathrm{D}}}}{a} \\ C_2 = \dfrac{2\pi}{F_{\mathrm{cD}}\cdot s}\dfrac{e^{ax_{1\mathrm{D}}}}{a}e^{2ax_{2\mathrm{D}}} \end{cases} \tag{B.15}$$

Thus, the fracture region pressure solution at the constant-pressure boundary conditions is

$$\overline{m}_{\mathrm{fD}}(x_{\mathrm{D}}) = -\frac{2\pi}{F_{\mathrm{cD}} \cdot s}\frac{\mathrm{e}^{ax_{1\mathrm{D}}}}{a}\left(\mathrm{e}^{ax_{\mathrm{D}}} - \mathrm{e}^{2ax_{2\mathrm{D}}-ax_{\mathrm{D}}}\right) \tag{B.16}$$

where $\overline{m}_{\mathrm{fD}}(x_{\mathrm{D}})$ is the G in Eqs. (13)–(15).

References

Ahmadi, M.A., Ebadi, M., Marghmaleki, P.S., Fouladi, M.M., 2014. Evolving predictive model to determine condensate-to-gas ratio in retrograded condensate gas reservoirs. Fuel 124, 241–257. https://doi.org/10.1016/j.fuel.2014.01.073.

Ai, S., Pang, W., Du, J., Liu, M., Tabish Haider, S., 2023. An analytical model for pressure transient behavior of acid-fractured well in fracture-cave oil reservoir: A field example from Tarim Basin in China. In: Middle East Oil, Gas and Geosciences Show. https://doi.org/10.2118/213478-MS.

Arbogast, T., Gomez, M.S.M., 2009. A discretization and multigrid solver for a Darcy–Stokes system of three dimensional vuggy porous media. Comput. Geosci. 13 (3), 331–348. https://doi.org/10.1007/s10596-008-9121-y.

Bourdet, D., Ayoub, J.A., Plrard, Y.M., 1989. Use of pressure derivative in well-test interpretation. SPE Form. Eval. 4 (2), 293–302. https://doi.org/10.2118/12777-PA.

Du, X., Lu, Z., Li, D., Xu, Y., Li, P., Lu, D., 2019. A novel analytical well test model for fractured vuggy carbonate reservoirs considering the coupling between oil flow and wave propagation. J. Petrol. Sci. Eng. 173, 447–461. https://doi.org/10.1016/j.petrol.2018.09.077.

Du, X., Li, Q., Li, P., Xian, Y., Zheng, Y., Lu, D., 2022. A novel pressure and rate transient analysis model for fracture-caved carbonate reservoirs. J. Petrol. Sci. Eng. 208, 109609. https://doi.org/10.1016/j.petrol.2021.109609.

Gao, B., Huang, Z., Yao, J., Lv, X., Wu, Y., 2016. Pressure transient analysis of a well penetrating a filled cavity in naturally fractured carbonate reservoirs. J. Petrol. Sci. Eng. 145, 392–403. https://doi.org/10.1016/j.petrol.2016.05.037.

Golfier, F., Lasseux, D., Quintard, M., 2015. Investigation of the effective permeability of vuggy or fractured porous media from a Darcy-Brinkman approach. Comput. Geosci. 19 (1), 63–78. https://doi.org/10.1007/s10596-014-9448-5.

Gringarten, A.C., 2008. From straight lines to deconvolution: The evolution of the state of the art in well test analysis. SPE Reservoir Eval. Eng. 11 (2), 363–388. https://doi.org/10.2118/102079-PA.

Hegeman, P.S., Hallford, D.L., Joseph, J.A., 1993. Well-test analysis with changing wellbore storage. SPE Form. Eval. 8 (3), 201–207. https://doi.org/10.2118/21829-PA.

Huang, Z., Xing, H., Zhou, X., You, H., 2020. Numerical study of vug effects on acid-rock reactive flow in carbonate reservoirs. Adv. Geo-Energy Res. 4 (4), 448–459. https://doi.org/10.46690/ager.2020.04.09.

Karimi-Fard, M., Durlofsky, L.J., Aziz, K., 2004. An efficient discrete-fracture model applicable for general-purpose reservoir simulators. SPE J. 9, 227–240. https://doi.org/10.2118/88812-PA.

Li, Q., Du, X., Tang, Q., Xu, Y., Li, P., Lu, D., 2021. A novel well test model for fractured vuggy carbonate reservoirs with the vertical bead-on-a-string structure. J. Petrol. Sci. Eng. 196, 107938. https://doi.org/10.1016/j.petrol.2020.107938.

Li, X., Huang, X., Yu, S., Lu, D., Du, X., 2023. Numerical study on the transient pressure response of the vug in carbonate reservoirs. Petrol. Sci. Technol. 42 (22), 3264–3283. https://doi.org/10.1080/10916466.2023.2190772.

Liao, T., Hou, J., Chen, L., Ma, K., Yang, W., Dong, Y., 2015. Evolutionary model of the Ordovician karst reservoir in Halahatang oilfield, northern Tarim Basin. Acta Pet. Sin. 36 (11), 1380–1391 (in Chinese).

Lin, J., Li, L., Yang, H., 2007. Primary investigation of the coupling of channel flow with seepage. J. Xi'an Shiyou Univ. (Natural Science Edition) 2, 11–15 +174 (in Chinese).

Liu, Z., 2020. Well Test Study for Fractured Vuggy Carbonate Reservoir Based on Non-continuous Medium Theory. Master's Thesis. Southwest Petroleum University (in Chinese).

Loucks, R.G., 1999. Paleocave carbonate reservoirs: Origins, burial-depth modifications, spatial complexity, and reservoir implications. AAPG (Am. Assoc. Pet. Geol.) Bull. 83 (11), 1795–1834. https://doi.org/10.1306/E4FD426F-1732-11D7-8645000102C1865D.

Mohammed, I., Olayiwola, T.O., Alkathim, M., Awotunde, A.A., Alafnan, S.F., 2021. A review of pressure transient analysis in reservoirs with natural fractures, vugs and/or caves. Pet. Sci. 18 (1), 154–172. https://doi.org/10.1007/s12182-020-00505-2.

Pan, Q., Cheng, L., Wang, B., Zhao, H., Jia, P., Jia, Z., Cao, C., 2024. Practical semi-analytical models for pressure-transient analysis of carbonate reservoirs with complex fracture and cave distributions. Energy Fuels. 38 (5), 3916–3926. https://doi.org/10.1021/acs.energyfuels.3c04130.

Stehfest, H., 1970. Algorithm 368: Numerical inversion of Laplace transforms. Commun. ACM 13 (1), 47–49. https://doi.org/10.1145/361953.361969.

Tang, X., Wu, D., Qiao, J., Gao, F., Zhang, M., 2023. Combining machine learning and physics modelling to determine the natural cave property with fracturing curves. Comput. Geotech. 158, 105339. https://doi.org/10.1016/j.compgeo.2023.105339.

Warren, J.E., Root, P.J., 1963. The behavior of naturally fractured reservoirs. Soc. Petrol. Eng. J. 3 (3), 245–255. https://doi.org/10.2118/426-PA.

Wei, C., Cheng, S., Song, J., Shi, D., Shang, R., Zhu, L., Yu, H., 2022. Pressure transient analysis for wells drilled into vertical beads-on-string caves in fracture-caved carbonate reservoirs: Field cases in Shunbei Oilfield. J. Petrol. Sci. Eng. 208, 109280. https://doi.org/10.1016/j.petrol.2021.109280.

Wu, B., Sun, W., Cai, G., Meng, G., 2022. Reliability analysis of shallow-buried tunnel construction adjacent to karst cave. Comput. Geotech. 145, 104673. https://doi.org/10.1016/j.compgeo.2022.104673.

Xu, G., Yin, H., Zhang, D., Fu, J., Xing, C., 2023. Numerical well test model of oil-water two-phase flow in fractured and vuggy carbonate reservoir. Adv. Geo-Energy Res. 10 (2), 91–103. https://doi.org/10.46690/ager.2023.11.04.

Yang, M., Huang, S., Zhao, F., Sun, H., Chen, X., 2024. Experimental investigation of CO_2 huff-n-puff in tight oil reservoirs: Effects of the fracture on the dynamic transport characteristics based on the nuclear magnetic resonance and fractal theory. Energy 294, 130781. https://doi.org/10.1016/j.energy.2024.130781.

Zhao, W., Shen, A., Qiao, Z., Zheng, J., Wang, X., 2014. Carbonate karst reservoirs of the Tarim Basin, northwest China: Types, features, origins, and implications for hydrocarbon exploration. Interpretation 2 (3), SF65–SF90. https://doi.org/10.1190/INT-2013-0177.1.